JOURNAL OF AIRCRAFT
Vol. 44, No. 4, July–August 2007

Adaptive Airfoil Dynamic Stall Control

Michael Kerho*
Rolling Hills Research Corporation, El Segundo, California 90245

DOI: 10.2514/1.27050

The purpose of this study was to investigate an adaptive airfoil design to alleviate, or greatly reduce, the negative effects of dynamic stall on rotorcraft blades. The adaptive airfoil design uses compliant structures technology to design an aerodynamically smooth, variable droop leading edge for airfoil dynamic stall control. The research presented here will focus on the numerical predictions of the aerodynamic performance of the adaptive leading edge. Both steady and unsteady time-accurate numerical predictions for a two-dimensional pitching and deforming airfoil were performed using a modified version of the Navier–Stokes solver OVERFLOW. The OVERFLOW code was modified to allow for a dynamically deforming grid system and variable Mach number capability. Numerical simulations were obtained with increasing complexity: from a simple fixed Mach number with a sinusoidal pitch cycle through a prescribed pitch distribution with fully variable Mach and a dynamically deforming airfoil. Results obtained to date indicate that the variable droop/camber compliant leading-edge system can achieve a higher $C_{l\max}$ than a baseline section, or eliminate the dynamic stall vortex at a C_l equivalent to the baseline section $C_{l\max}$ while maintaining the baseline section's high Mach number advancing blade characteristics.

Nomenclature

C_d	=	drag coefficient, $D/0.5\rho U_\infty^2$
C_l	=	lift coefficient, $L/0.5\rho U_\infty^2$
C_m	=	pitching moment coefficient, $M/0.5\rho U_\infty^2 c$
c	=	airfoil chord length
k	=	reduced frequency, $\omega c/2U_\infty$
M_{body}	=	unsteady Mach number component
M_{fixed}	=	static freestream Mach number component
M_{tot}	=	total equivalent freestream Mach number for unsteady mixed reference fixed $= M_{\text{frame}} + M_{\text{body}}$
M_∞	=	freestream Mach number
R	=	rotor blade radius
r	=	rotor blade radial coordinate
U_∞	=	freestream velocity, ft/s
α	=	angle of attack, deg
μ	=	advance ratio, M_∞/M_{tip}
ψ	=	rotor azimuth, deg (0 aft)
ω	=	pitch rate, rad/s

Introduction

FOR fixed wing aircraft, wing stall limits the low speed characteristics of the aircraft. For rotorcraft, however, retreating blade stall is the primary limiting factor affecting the high-speed characteristics and payload capability of the aircraft. During forward flight, the advancing rotor blade encounters increased velocity due to the combination of the rotational velocity of the rotor combined with the rotorcraft's forward speed. Conversely, the retreating blade experiences a decreased velocity. To maintain level, coordinated flight, the lift generated from the retreating blade must equal that of the advancing blade. To achieve balanced lift across the rotor disk as speed increases, the angle of attack of the retreating blade must increase due to its lower relative velocity. Simultaneously, the advancing blade has a higher relative velocity and must decrease in angle of attack to maintain constant lift. At some forward speed, the increasing angle of attack of the retreating blade will cause it to stall. The tendency for the retreating blade to stall in forward flight is inherent in all present day rotorcraft and is a major factor in limiting their forward speed and maneuverability [1]. The retreating blade stall causes buffeting and vibration at critical airspeeds. Large negative pitching moments are also observed. Because the blades are normally flexible, the pitching moment change also poses aeroelastic problems. Figure 1 shows a representative schematic of the angle of attack and stall distribution for a typical rotorcraft blade system in forward flight.

In addition to the essentially static stall of the retreating blade at higher forward velocities, the dynamics of the pitching blade introduce additional problems. When an airfoil is pitched up rapidly, as it does as the blade rotates from the advancing side to the retreating side, it is possible to overshoot the static $C_{l\max}$ and achieve a significantly higher $C_{l\max(\text{Dynamic})}$. In addition, when the airfoil is then pitched back down, or held at a constant angle of attack, there is a corresponding decrease in lift that extends below the static value. This characteristic lift overshoot has been observed in both fixed wing and rotary wing aircraft for many years. For the case of a traditional airfoil, an overshoot above the static $C_{l\max}$ occurs in the pitch cycle due to the formation of a large vortex on the airfoil upper surface that separates and travels downstream. The final breakdown in C_l for the section occurs when this vortex has traveled past the trailing edge. At this point, the flow is massively separated and the lift drops to levels far below those typical of the static curve, requiring a significant reduction in angle of attack before reattachment. The movement of the vortex, or dynamic stall vortex, from the airfoil leading to trailing edge, results in a large change in section pitching moment, becoming increasingly negative (nose-down) as the vortex reaches the trailing edge. Although the dynamic lift provides a benefit in $C_{l\max}$, the more severe stall that follows further limits the performance of the helicopter blade system.

Many avenues have been explored in an attempt to overcome the limitations imposed by retreating blade stall. Airfoils are selected to provide high lift, low drag, and a near zero pitching moment to reduce control moments. The blade tips are often twisted, or washed-out, to provide lower angles of attack at the tips. The airfoil section itself can be varied across the blade span to smooth out the lift distribution. Generally, a tradeoff is made between the performance of the advancing blade vs the retreating blade. Variable geometry airfoils are a good method of optimizing the airfoil shape for the local flow conditions as the blade rotates. These variable shape/camber sections have proven effective in both experimental and numerical studies [2–6]. For a rotorcraft application where the airfoil is pitched up in angle

Presented as Paper 1365 at the 43rd AIAA Aerospace Sciences Meeting, Reno, Nevada, 10–14 January 2005; received 4 August 2006; revision received 29 September 2006; accepted for publication 29 September 2006.

*Chief Aerodynamicist, 420 North Nash Street; mike@rollinghillsresearch.com. AIAA Associate Fellow.

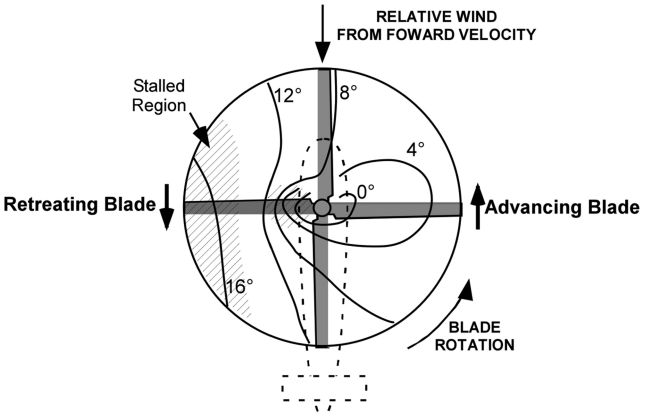

Fig. 1 Angle of attack and stall distribution in forward flight [1,18].

of attack, the leading or trailing edge of the airfoil is dynamically deformed at different angles of incidence. The new deformed airfoil shape is better able to deal with the large adverse pressure gradients created by the suction peak generated by the high section incidence. Dynamically drooped leading edges have been shown to significantly reduce or eliminate the massive flow separation and the dynamic stall vortex for a given angle-of-attack condition [5,7]. Although experimental and computational results have shown great promise for variable camber geometries, traditionally variable geometry airfoils, such as the mission adaptive wing [8], have been very complex structurally and consequently heavy and maintenance intensive, and are not appropriate for the confined space requirements and harsh operating environment of a rotor blade. Another significant challenge for a variable camber rotor section is the fact that the camber change must happen cyclically with the blade rotation. This periodic change in the blade shape must occur on the order of 5–7 Hz. The severely constrained space requirements, coupled with the frequency of operation and high g rotational environment, have made a variable camber blade section impractical. Recent advances in the design of compliant smart structures technology, however, have made the possibility of a reliable and robust variable camber blade section that can operate at the required frequencies a reality. A significant advantage offered through the use of compliant smart structures is the ability to dynamically shape both the advancing and retreating blades. Whereas the retreating blade can be optimized for high lift and delay of dynamic stall, the advancing blade can be optimized to provide better transonic performance, allowing the possibility for increased performance across the flight envelope. Another significant advantage of a compliant structure geometry is the ability to generate the leading-edge droop with a smooth aerodynamic surface, avoiding hinge line seals and disruptions.

The purpose of the current project is to attempt to exploit the aerodynamic benefits associated with deformable compliant structures to produce a variable camber leading edge for dynamic stall control. Although the current project is a multidisciplinary design approach, coupling the structural and aerodynamic design, only the numerical simulations involved in the aerodynamic design will be discussed here.

Geometry

The baseline airfoil used in this study was the Sikorsky SSC-A09 section. The SSC-A09 is representative of a modern rotorcraft blade section which performs well at transonic conditions but could use some reshaping for better dynamic stall performance. One of the key aspects of the current study was to produce a structurally realistic aerodynamic design. Because most modern rotorcraft blade sections have a D-spar located at the leading edge of the airfoil, this D-spar must be moved aft to allow space for the deformation mechanism. From a stiffness and balance point of view, the aft movement of the D-spar must be minimized. There must be sufficient space in front of the D-spar, however, to provide for a reasonable camber change and droop deflection to maximize the aerodynamic benefit. In addition to minimizing the movement of the D-spar, it was also sought to minimize the droop angle of the leading edge. The overall design sought to maximize the aerodynamic benefit while minimizing both the chordwise extent of the droop and the maximum droop angle. One of the designs studied drooped the leading edge 10 deg downward while moving the D-spar aft to the 8.5% chord location. The section is termed the Spar85Defl10. A schematic of the baseline and drooped SSC-A09 section is shown in Fig. 2. The actual deformation begins at approximately the 15% chord location. The structure is designed to continuously deform throughout the pitch cycle at a rate up to 7 Hz.

Numerical Methodology

Several compliant variable camber leading-edge designs have been studied numerically, both statically and dynamically. The compressible Reynolds-averaged Navier–Stokes computational fluid dynamics code OVERFLOW has been used for the numerical predictions in this study. The OVERFLOW code uses chimera overset (structured) grid systems and has been developed at NASA and applied to a wide range of both internal and external fluid dynamic problems. The OVERFLOW 1.8ab code was extensively modified to include the dynamically deforming grid and variable Mach capability. All analysis performed to date has been two-dimensional (2-D) using a single c-mesh grid.

A grid refinement study for the time-accurate simulations produced a grid with dimensions of 377×93 and a y+ of the first grid line off the surface on the order of one. To resolve the time-dependent features of the flowfield with sufficient accuracy and proper computational convergence, approximately 30,000 time steps per oscillation were used with three Newton subiterations. The use of up to six Newton subiterations was also investigated but found to provide identical results to the three subiterations. Solutions were run for a period of 2.5 cycles to provide sufficient periodic convergence. All cases were run fully turbulent using Roe upwinding and the

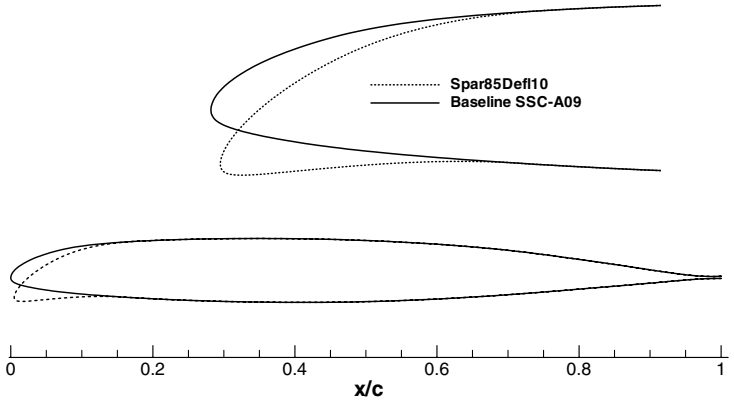

Fig. 2 Comparison of baseline SSC-A09 and 10 deg compliant drooped Spar85Defl10 section.

Spalart–Allmaras (SA) turbulence model. The SA model has been shown to be effective and robust for a variety of flows including 2-D separated airfoil flows [9,10].

Grid Deformation

The deforming grid capability allows the leading edge of the airfoil to droop dynamically throughout the pitch cycle providing a more realistic performance prediction. Several routines within OVERFLOW were extensively modified to include the deformation routines. Additionally, a new input deck was added to the OVERFLOW code to allow the unsteady input variables (reduced frequency, pitch amplitude, droop schedule, etc.) to be specified in the input file. Through the input deck, the routines can be specified to use a simple sinusoidal pitch cycle, or a user supplied pitch cycle can be specified (α vs ψ) and read in during startup. Similarly, the surface deformation is handled in the same manner. A simple sinusoidal deformation scheme with specified limits and chordwise extents, or a user supplied deformation schedule, can be read in during startup.

The deforming grid capability added to the OVERFLOW code is rather generic and robust in that the method could be rather easily extended to a three-dimensional (3-D) or multigrid system. In order for the deforming grid capability to be easily extended to 3-D or a multigrid overset system, it would be beneficial for some cases to avoid having to recalculate the intergrid connectivity after every grid deformation. It would be more desirable to allow individual grids to deform while maintaining their outer boundary without any movement of the overlap regions. This type of deformation strategy was employed in the current study. The method is similar to and was modeled after that proposed by Morton et al. [11] with modifications made to handle a c-mesh.

The most common grid or mesh deformation strategy in use is transfinite interpolation (TFI). TFI is popular due to its algebraic nature and low computational cost. TFI schemes may be as simple as connecting surfaces with straight lines in the body normal direction and preserving arc-length between nodes or, more usually, a simple linear distribution of transnational displacements [11]. The drawback in using a TFI scheme is that generally they do not guarantee grid orthogonality at the body surface, a desirable quality for Navier–Stokes viscous flow simulations. The strategy developed by Morton et al. [11] is similar to TFI in that its approach in redefining the normal grid lines is algebraic. Grid quality and orthogonality of the mesh at the surface, however, is maintained. The approach also limits deformation to a specified region of the grid, allowing the outer far-field regions to be held fixed, maintaining overlap and connectivity. The strategy is relatively robust and allows for large surface deformations.

From Morton et al. [11], for an initial grid and surface displacement, the translation and rotation of each surface node is computed from the deformed aerodynamic surface. Each normal grid line is then moved in a rigid-body fashion according to the displacement and rotation of the surface node to form a reference, displaced grid line. The new grid line is then constructed by blending the reference grid line and the undeformed grid line. A cubic blending with zero slope at the end point assures both that any initial wall orthogonality or grid quality is maintained and that the grid transitions smoothly in the far field. This method of grid deformation is used to deform the leading-edge area of the airfoil and also for changes in angle of attack for all dynamic solutions. An example of the SSC-A09 grid undergoing a leading-edge deflection from 0 to 10 deg droop for α from 0 to 20 deg is shown in Fig. 3. From Fig. 3, the deformation routine produces a smooth transition throughout the deformation. Most important, however, is that the grid mesh orthogonality is maintained at the surface.

Because of the deforming nature of the grid, use of the geometric conservation law (GCL) [12] in the flow solver was also investigated. To maintain global conservation for fluid dynamic numerical solutions involving body conforming coordinate transformations,

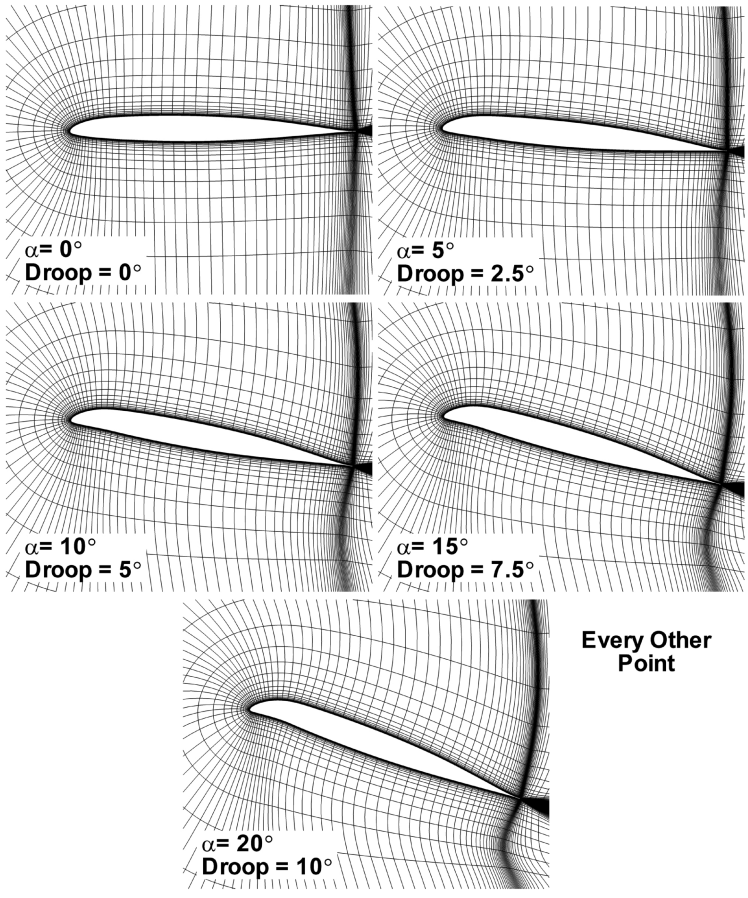

Fig. 3 Progressive grid deformation for the SSC-A09 section undergoing pitch and nose droop.

spatial and temporal grid metrics must satisfy certain geometric identities [13,14]. If the GCL is not satisfied, inaccuracies and or instabilities in the solution may result. Modifications were made to the OVERFLOW code to satisfy the GCL and time-accurate fully deforming cases were run with and without GCL to determine its effect. Although being the most correct form of the numerical solution, inclusion of the GCL in the flow solver produced results that were within plotting accuracy when compared with solutions generated without the GCL implementation. This is most likely a result of the small time steps used coupled with the fact that the basic OVERFLOW formulation includes freestream subtraction. Because no noticeable differences were observed between the baseline and GCL implementation, GCL was not used due to its additional computational cost.

Unsteady Mach Capability

In addition to the deforming grid capabilities of the modified code, the ability to vary the Mach number throughout the pitch cycle was added to the modified OVERFLOW code. The varying Mach number more closely mimics the rotational behavior of the rotorcraft blade in forward flight. The variation in Mach throughout the pitch cycle can be quite significant, from transonic values on the advancing blade ($M \approx 0.75$) to low values on the retreating blade ($M \approx 0.3$). The varying Mach capability allows the both the high-speed advancing blade characteristics and low-speed high-lift retreating blade characteristics to be studied in the same run. A rather simple and elegant solution was arrived at for varying the Mach number. Instead of physically moving the grid to simulate the varying speed of the rotating blade, the time metric for the grid was modified. By modifying the time metric for the grid, the code sees a variation in grid speed without the grid actually moving. As a result, the grid boundaries remain constant, but the surface appears to be moving. Instead of the reference system where the body remains fixed in space and flow moves, the code thinks the body is translating in the direction of the freestream flow, producing an additive velocity to the freestream.

Several test cases were run to verify the modified Mach number capability. For example, the baseline SSC-A09 section was run statically in a fixed reference frame at $\alpha = 0\,\text{deg}$, $M_\infty = 0.70$ and compared with a mixed reference frame time-accurate varying Mach number case with an equivalent freestream Mach number. For the mixed reference frame equivalent Mach number case, a fixed freestream Mach number of $M = 0.4$ was used with an unsteady varying component of 0.3, yielding a total Mach number of $M = 0.70$ ($M_{\text{tot}} = M_{\text{fixed}} + M_{\text{body}}$). For the varying Mach number time-accurate cases, force and moment values are nondimensionalized by the instantaneous dynamic pressure for that given time step. The pressure distributions for the static, fixed reference frame $M_\infty = 0.70$ and the time-accurate mixed reference frame, $M_\infty = 0.40_{\text{fixed}} + 0.30_{\text{body}} = 0.70$ cases are shown in Fig. 4. From Fig. 4, the static and time-accurate mixed reference frame unsteady Mach pressure distributions are identical. The modified code correctly accounts for the added Mach number capability in both the flow solver and reduction routines.

Numerical Validation

To provide some validation of the modified OVERFLOW results, numerical and experimental unsteady results for the NACA 0012 are compared. The experimental results are those of Wood [15] for a sinusoidal pitch cycle, $\alpha = 6.25 + 8.5\,\text{deg}\,\sin(\omega t)$. Unsteady experimental and OVERFLOW lift curve and pitching moment results for the NACA 0012 section at a reduced frequency of $k = 0.075$, $M = 0.40$, and $Re = 3.4 \times 10^6$ are shown in Fig. 5. From Fig. 5, the C_l results compare relatively well with the measured data. Lift levels on the upstroke are slightly underpredicted, but $C_{l\,\max}$ and the angle at which it occurs are in good agreement. OVERFLOW also predicts lower lift on the downstroke until reattachment. From the pitching moment results, OVERFLOW overpredicts the magnitude of the negative pitching moment due to the passage of the dynamic stall vortex. Overall, the unsteady time-accurate OVERFLOW results compare relatively well with the experimental data.

Results

Unsteady time-accurate results for the baseline SSC-A09 and compliant adaptive Spar85Defl10 sections will be presented in two groups. The first group represents traditional sinusoidal forced oscillations at a fixed Mach number. The second group of results represents a more realistic rotorcraft blade environment. Instead of the sinusoidal pitch oscillation, both the pitch and Mach history are prescribed as a function of the blade rotation angle. The pitch history is derived from comprehensive rotorcraft analysis results obtained from a CAMRAD II analysis of a UH-60A Blackhawk helicopter. This more realistic pitch history is coupled with a variable Mach number which more closely mimics the rotational behavior of the rotorcraft blade in forward flight.

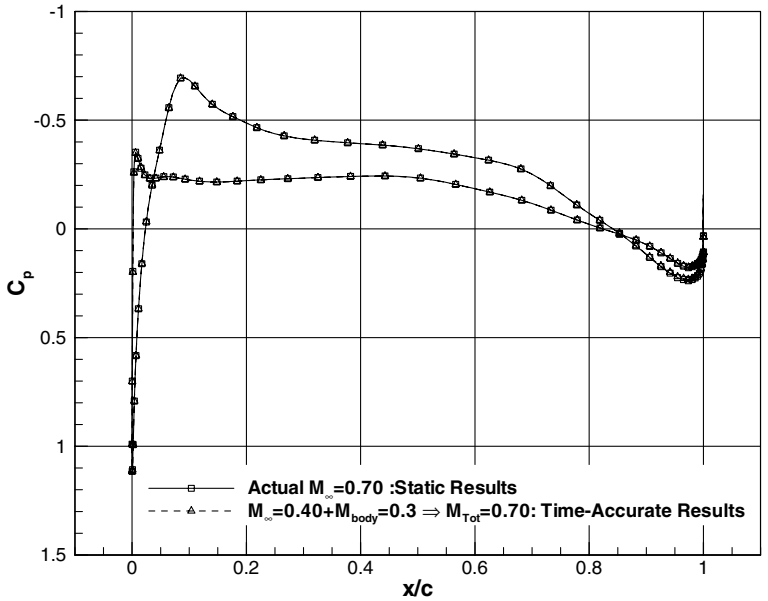

Fig. 4 Static baseline OVERFLOW surface pressure and unsteady Mach time-accurate results for the baseline SSC-A09, $\alpha = 0\,\text{deg}$.

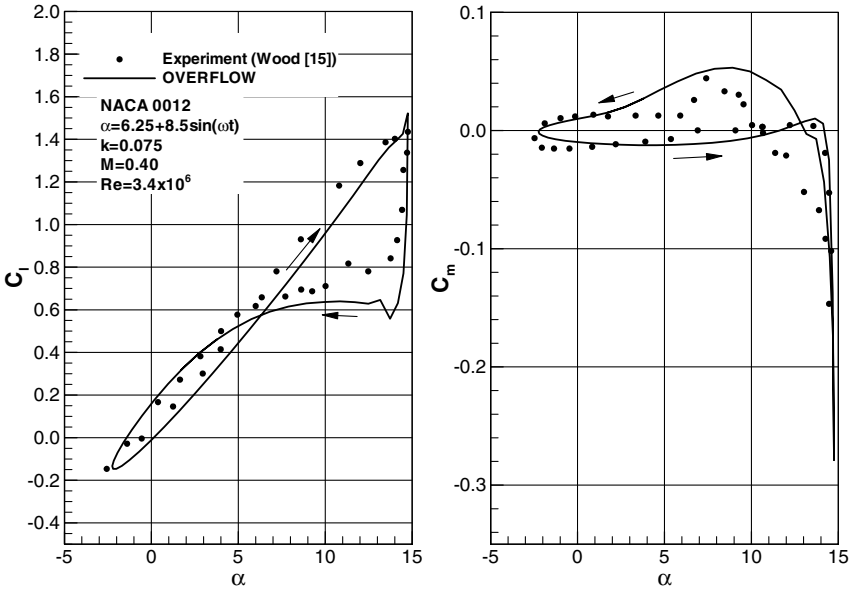

Fig. 5 Forced oscillation time-accurate OVERFLOW and experimental data for a NACA 0012.

Sinusoidal Oscillations

Dynamic lift curve results for the baseline SSC-A09 section and the compliant adaptive section (Spar85Defl10) undergoing a sinusoidal pitch cycle with $\alpha = 10 + 10\,\text{deg}\ \sin(\omega t)$, $k = 0.075$, $M = 0.40$ are shown in Fig. 6. As was discussed in the geometry section, the maximum droop angle set for the geometry was 10 deg. The droop schedule for the compliant adaptive section follows a sinusoidal deflection schedule based on the same frequency as the angle-of-attack schedule, providing a 0–10 deg deflection for a pitch cycle angle-of-attack range from 0–20 deg, $\alpha_{\text{droop}} = 5 + 5\,\text{deg}\ \sin(\omega t)$. From Fig. 6, the difference in the dynamic results between the baseline SSC-A09 section and the drooped Spar85Defl10 section are dramatic. The baseline SSC-A09 section stalls at approximately 17 deg with a $C_{l\max} = 1.9$, followed by increasing separation with increasing α. The variable camber section, however, does not stall until approximately 19.5 deg with a $C_{l\max}$ of 2.1. The character of the stall is also different. The baseline SSC-A09 section $C_{l\alpha}$ increases in slope before reaching $C_{l\max}$, whereas the adaptive section C_l reaches a slight plateau before increasing sharply just before reaching its $C_{l\max}$. These differences are due to the nature of the separation. For the SSC-A09 section, the separation is shock-induced and begins near the leading edge. The increase in slope before $C_{l\max}$ is the formation and shedding of the dynamic stall vortex. For the variable camber section, however, separation begins at the trailing edge and moves forward before a vortex forms. The slight plateau in C_l before increasing before $C_{l\max}$ is the onset of trailing-edge separation. The sharp increase in C_l is due to the vortex that forms and sheds as separation moves quickly forward. The leading-edge droop of the Spar85Defl10 section reduces the leading-edge pressure peak and avoids the resulting shock-induced separation experienced by the baseline SSC-A09 section. These differences in stall characteristics also affect the drag and pitching moment behavior. Both the drag and pitching moment results show markedly better behavior for the drooped section throughout the baseline SSC-A09 stall range with the large negative pitching moment and drag rise associated with the formation, shedding, and passage of the dynamic stall vortex delayed well beyond the baseline SSC-A09. Upon separation and shedding of the dynamic stall vortex, the variable camber section does produce spikes in the drag and pitching moment beyond those of the baseline SSC-A09 section. It

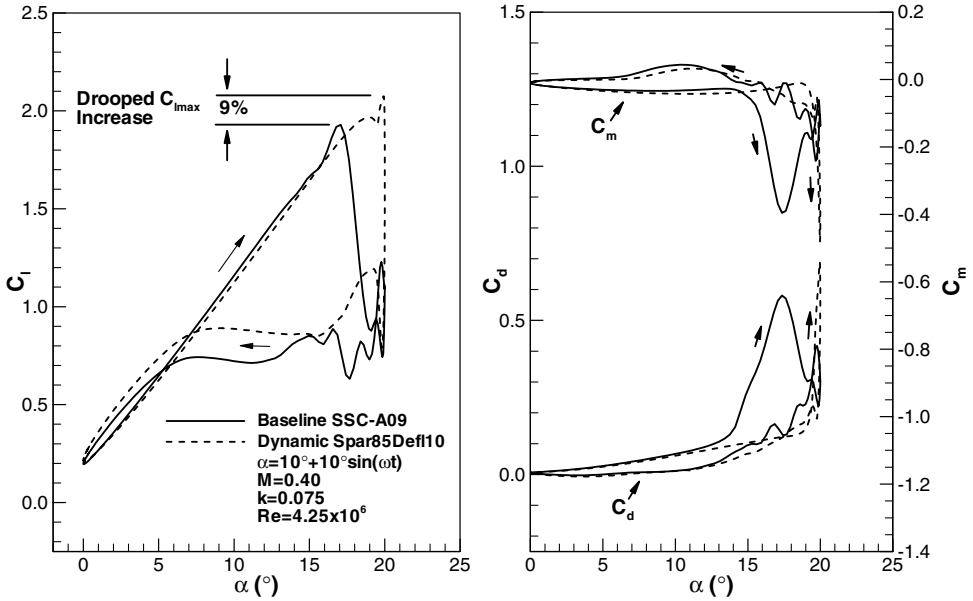

Fig. 6 Force and moment polars for a sinusoidal dynamic pitch loop, $\alpha = 10 + 10\,\text{deg}\ \sin(\omega t)$.

should also be noted that the low α upstroke behavior of the adaptive and SSC-A09 sections are identical. As a result, there should be no aerodynamic penalty incurred by the adaptive section on the advancing blade. For the current case ($\alpha = 10 + 10\,\text{deg}\ \sin(\omega t)$, $k = 0.075, M = 0.40$), the complete suppression of the dynamic stall vortex might be accomplished by increasing either the chordwise extent of the droop or the droop angle. For a similar pitch cycle and freestream conditions, Chandrasekhara et al. [7] was able to completely suppress formation of the dynamic stall vortex using a VR-12 section with a simple 25% chord variable droop leading-edge flap with a maximum droop angle of 20 deg. The increased chordwise extent of the flap and larger droop angle, as compared with the Spar85Defl10 section of the current study were able to suppress the formation of the dynamic stall vortex to a higher angle of attack.

From the dynamic results shown in Fig. 6, the Spar85Defl10 drooped geometry is clearly capable of providing an increased $C_{l\max}$ and stall angle. The main objective, however, was to produce a section that can alleviate or eliminate the shedding of the dynamic stall vortex to an angle of attack and lift coefficient significantly higher than the baseline section. Because the previous results were run with a mean α of 10 deg, with a 10 deg amplitude, the baseline and Spar85Defl10 section were rerun, limiting the max α to 17 deg, $\alpha = 8.5 + 8.5\,\text{deg}\ \sin(\omega t)$ to see if the shedding of the dynamic stall vortex could be eliminated. Pitch loop results for these cases are shown in Fig. 7. From Fig. 7, the C_l pitch loop results for the Spar85Defl10 section clearly show a marked difference from the baseline SSC-A09 section. The drooped section appears to completely eliminate the shedding of the dynamic stall vortex while maintaining the baseline section $C_{l\max}$. No large lift loss is observed during the downstroke. These results are confirmed by the drag and pitching moment behavior. The large drag rise and negative pitching moment associated with the shedding of the dynamic stall vortex on the baseline section are absent from the drooped section results. These results are very encouraging. Not only can the compliant variable camber section eliminate the negative drag and pitching moment effects associated with the dynamic stall vortex, it can do so without any loss in $C_{l\max}$.

Contours of Mach number for the baseline SSC-A09 and dynamically deformed section at different points throughout the pitch cycle are shown in Fig. 8. Also included in Fig. 8 are contours of zero u velocity. The $u = 0$ contours simply depict the location above the model surface that separates reversed flow from the flow in the streamwise direction. The contours provide a simple mechanism for visually identifying the onset of separation, be it shock-induced near the leading edge, or basic trailing-edge separation. Again, it should be noted that the results presented are 2-D. For a strictly 2-D flowfield, aft of the stagnation point on the upper surface, reverse flow indicates separation. From Fig. 8, the large areas of reverse flow associated with the separation and passage of the dynamic stall vortex for the baseline SSC-A09 section are clearly evident. The dynamically drooping Spar85Defl10 results, however, look markedly different. No large areas of reverse flow or formation of a dynamic stall vortex are observed. Only a small amount of trailing-edge reverse flow at the pitch loop apex and initial down stroke are evident. The dynamically deforming section appears to provide significant aerodynamic benefits when compared with the baseline SSC-A09 section by eliminating the formation and passage of the dynamic stall vortex while producing a slight increase in $C_{l\max}$.

Prescribed Pitch/Mach History

To better understand the blade rotational effects and produce a more accurate aerodynamic prediction, prescribed pitch and Mach histories were investigated. The pitch and Mach effects were studied in increasing complexity. First, the effect of a realistic pitch history was investigated as compared with the traditional sinusoidal variation. Next, the effect of a variable Mach number was added. The conditions for these unsteady runs simulate a heavy UH-60A operating at an advance ratio of $\mu = 0.33$, $M_\infty = 0.21$ at a blade radius of $r/R = 0.865$. The blade pitch history for the UH-60A case in question is that predicted by the comprehensive rotorcraft analysis code CAMRAD II [16] as determined by Bousman [17].

To best study the effects of having a varying Mach/α distribution, a set of unsteady runs were made where a constant Mach number with a sinusoidal pitch variation case is used as a baseline ($\alpha = 10 + 10\,\text{deg}\ \sin(\omega t)$, $M_\infty = 0.40$). This case is then compared against a case using constant Mach number ($M_\infty = 0.40$) with the CAMRAD II generated α variation. Finally, these results are compared with the case where both the CAMRAD II generated α schedule and variable Mach number for the UH-60A ($\mu = 0.33$, $M_\infty = 0.21$ at a blade radius of $r/R = 0.865$) are used. A comparison of the sinusoid/CAMRAD II α schedules and constant/variable Mach as a function of blade rotation angle is shown in Fig. 9.

From Fig. 9, both the sinusoid and CAMRAD II α schedules reach a minimum α around $\Psi = 90$ deg on the advancing side. As the blade rotates toward the retreating side, the sinusoid continues a smooth increase in incidence, whereas the CAMRAD II schedule increases at a much lower rate until approximately $\Psi = 230$ deg where the α increases rapidly, followed by an equally sharp descent. For the majority of the pitch cycle, the CAMRAD II schedule has an

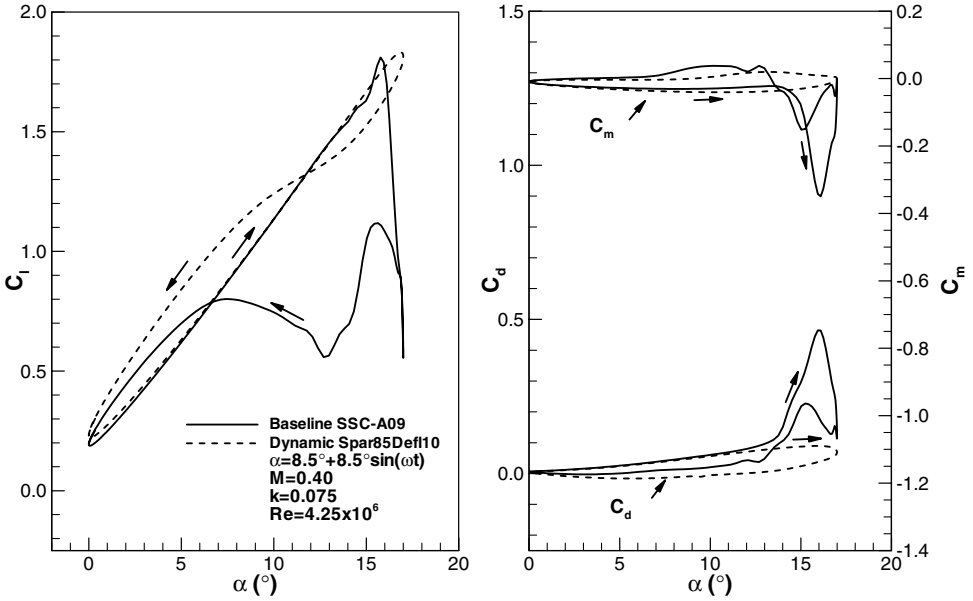

Fig. 7 Force and moment polars for a sinusoidal dynamic pitch loop, $\alpha = 8.5 + 8.5\,\text{deg}\ \sin(\omega t)$.

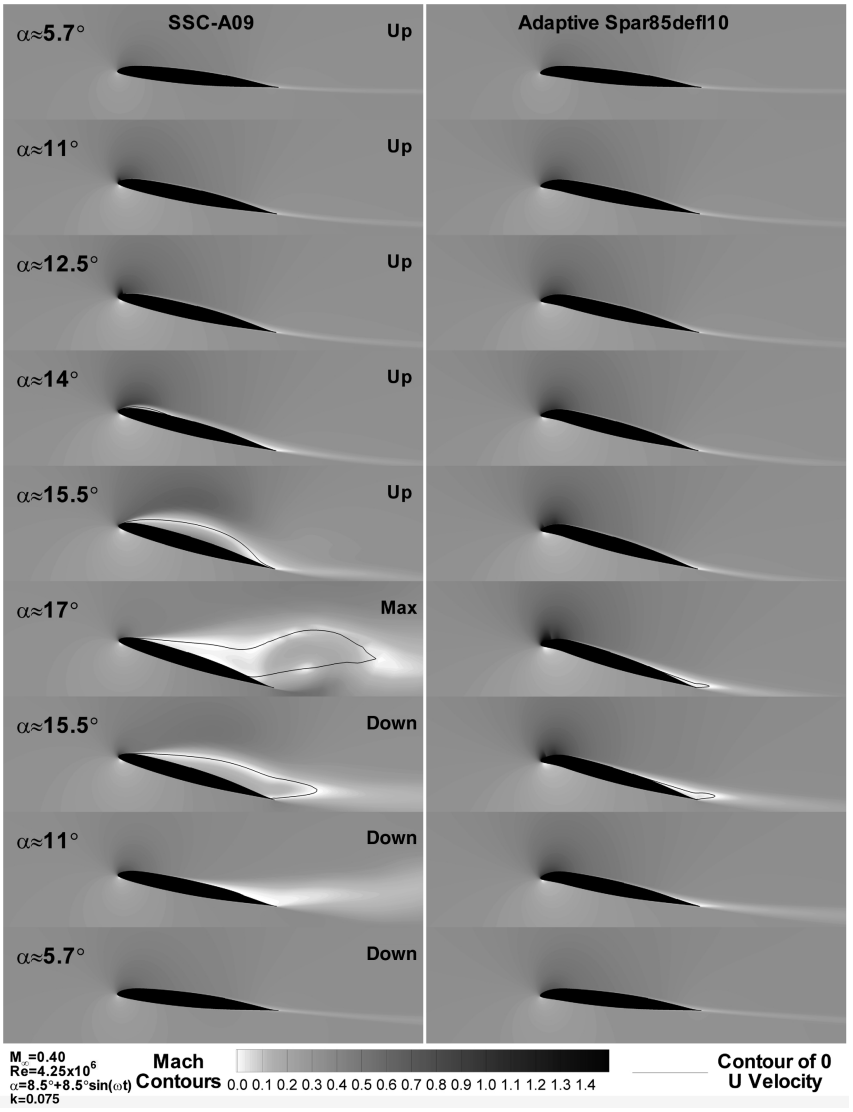

Fig. 8 Mach contours for the baseline SSC-A09 and dynamically drooping Spar85Defl10 section.

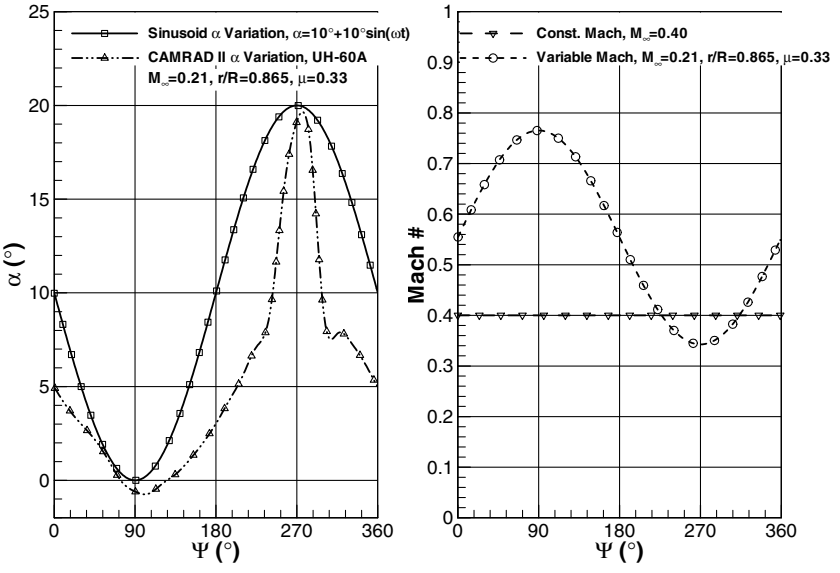

Fig. 9 Comparison of sinusoid and CAMRAD II α schedules and constant and variable Mach.

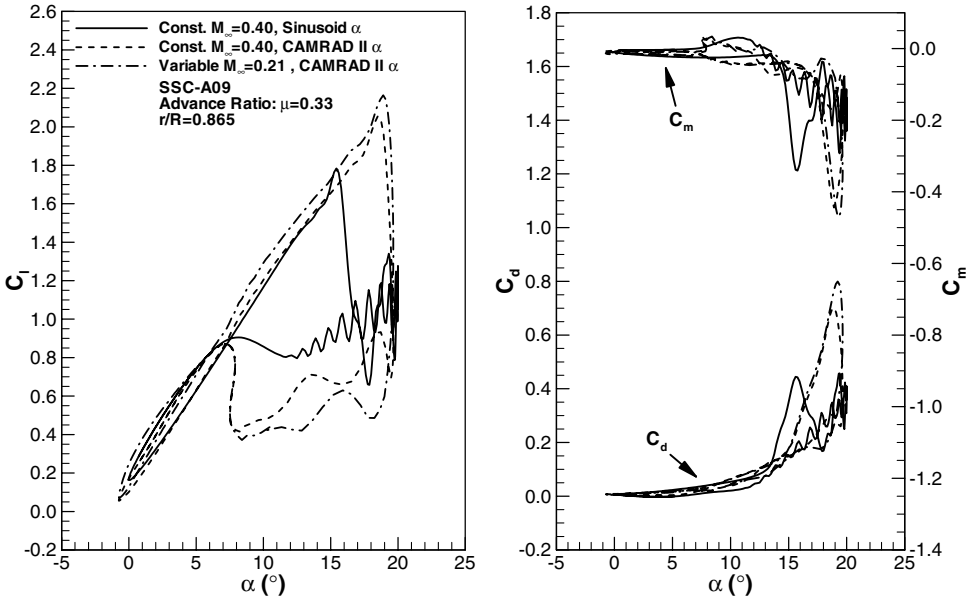

Fig. 10 Unsteady results for SSC-A09 showing effects of variable Mach and CAMRAD II α distributions.

effectively lower reduced frequency than the sinusoidal variation, with the exception being the rapid variation beginning at $\Psi = 230$ deg where the reduced frequency is significantly higher than the sinusoid schedule by approximately a factor of three. Because the blade rotational velocity is constant, the Mach variation with blade rotation is sinusoidal and 180 deg out of phase with the α schedule.

Force and moment results for the baseline sinusoidal α with constant Mach, the CAMRAD II α with constant Mach, and the CAMRAD II α with variable Mach are shown in Fig. 10. From Fig. 10, the difference between the sinusoidal α and CAMRAD II generated α schedules for a constant Mach number are quite significant. The sinusoidal case reaches a $C_{l\max} = 1.77$ at $\alpha = 15.5$ deg, with the CAMRAD II case reaching $C_{l\max} = 2.05$ at $\alpha = 18.4$ deg. The increased reduced frequency generated by the rapid α increase delays the separation of the dynamic stall vortex to a higher α, producing a significantly higher $C_{l\max}$, accompanied by a larger loss in lift on the downstroke. The effect of the variable Mach number is also significant, producing a higher C_l on the upstroke and a further increase in $C_{l\max}$. The increased C_l on the upstroke for the variable Mach result is due to compressibility effects. Although the Mach number on the upstroke is continually decreasing, the absolute Mach number for the variable Mach case is larger than that for the constant Mach number case throughout much of the upstroke (Fig. 9), producing an increased C_l. The increase in $C_{l\max}$ for the variable Mach case is due to two effects, both being related to the lower Mach number of the variable Mach case at the apex of the pitch cycle. At the apex of the pitch cycle, the Mach number for the variable Mach case is $M = 0.34$, as compared to $M = 0.40$ for the constant Mach case. The lower absolute Mach number will delay shock-induced separation until a higher angle of attack. The lower Mach number also produces a further effective increase in the reduced frequency. These two effects combine to produce a higher $C_{l\max}$ for the variable Mach case as compared with the fixed Mach case. Also of interest for the variable Mach number results shown in Fig. 10 is the fact that the C_l vs α curve is nonlinear on the upstroke. The nonlinear C_l vs α is the result of the continuously variable Mach number. Because the predicted aerodynamic forces and moments in the unsteady freestream Mach environment are normalized by the instantaneous conditions, the continual variation in Mach number on the upstroke produces a nonlinear variation in C_l. For cases involving the dynamically drooping leading edge of the Spar85Defl10 section, this nonlinearity is also effected by the continuous change in effective camber of the section as the nose droop angle continuously changes.

Unsteady contours of Mach number for the SSC-A09 with constant Mach and sinusoid pitch cycle are compared with the variable Mach and CAMRAD II pitch cycle in Fig. 11. Also included in Fig. 11 are contours of zero u velocity. Recall from Fig. 10, the constant Mach/sinusoid pitch case reaches its $C_{l\max}$ at approximately 15.5 deg, whereas the variable Mach/CAMRAD II case reaches its $C_{l\max}$ at 19 deg. From Fig. 11, for both cases, separation begins near the leading edge due to a shock. Separation then extends aft with the formation, growth, and passage of a dynamic stall vortex. For the constant Mach/sinusoid case, separation begins at approximately 12.5 deg. Because of the increased effective reduced frequency of the variable Mach/CAMRAD II case, separation onset is delayed until approximately 15.4 deg. The overall separation mechanism for both cases, however, appears to be similar and is shock induced. The increased pitch rate/reduced frequency of the variable Mach/CAMRAD II case simply delays the onset to a higher angle of attack.

After running the baseline SSC-A09 section with the new Mach/α schedules, the compliant droop geometry was investigated. The variable Mach/CAMRAD II pitch distribution results for the SSC-A09 section are compared with the adaptive airfoil Spar85Defl10 section results in Fig. 12. The conditions shown in Fig. 12 are again those for the UH-60A case, $\mu = 0.33$, $M_\infty = 0.21$ at a blade radius of $r/R = 0.865$. Previous comparisons of the dynamic behavior between the SSC-A09 and the adaptive Spar85Defl10 section showed a higher $C_{l\max}$ for the adaptive section. For the angle-of-attack range prescribed in the CAMRAD II pitch history, however, the SSC-A09 section is actually producing a slightly higher $C_{l\max}$ than the adaptive section. The reasons for this role reversal will become evident shortly. The SSC-A09 section produces a higher $C_{l\max}$ due to the fact that it is generating a much stronger, more pronounced dynamic stall vortex than the Spar85Defl10 section as evidenced by the C_d and C_m loops. Arrows denoting the pitch loop path for the SSC-A09 and Spar85Defl10 section are also included in Fig. 12. Upon closer examination, the breaks in the C_d and C_m curves denoting the formation and passing of the dynamic stall vortex occur at a significantly lower α for the SSC-A09 section as compared with the Spar85Defl10 section ($\approx$15–17 deg as compared with 19.6 deg). The Spar85Defl10 section is clearly remaining attached longer, and the larger $C_{l\max}$ produced by the SSC-A09 section comes at the expense of increased drag and negative pitching moment at a lower α. Unsteady contours of Mach number for the SSC-A09 and adaptive Spar85Defl10 section with the variable Mach and CAMRAD II pitch cycle are shown in Fig. 13. Also included in Fig. 13 are contours of zero u velocity. The Mach and reverse flow contours shown in Fig. 13 clearly show the SSC-A09 section generating a shock-induced separation near the leading edge on the upstroke beginning at approximately $\alpha \approx$ 15–17 deg. Separation then extends aft with increasing angle of attack with the formation, growth, and passage of

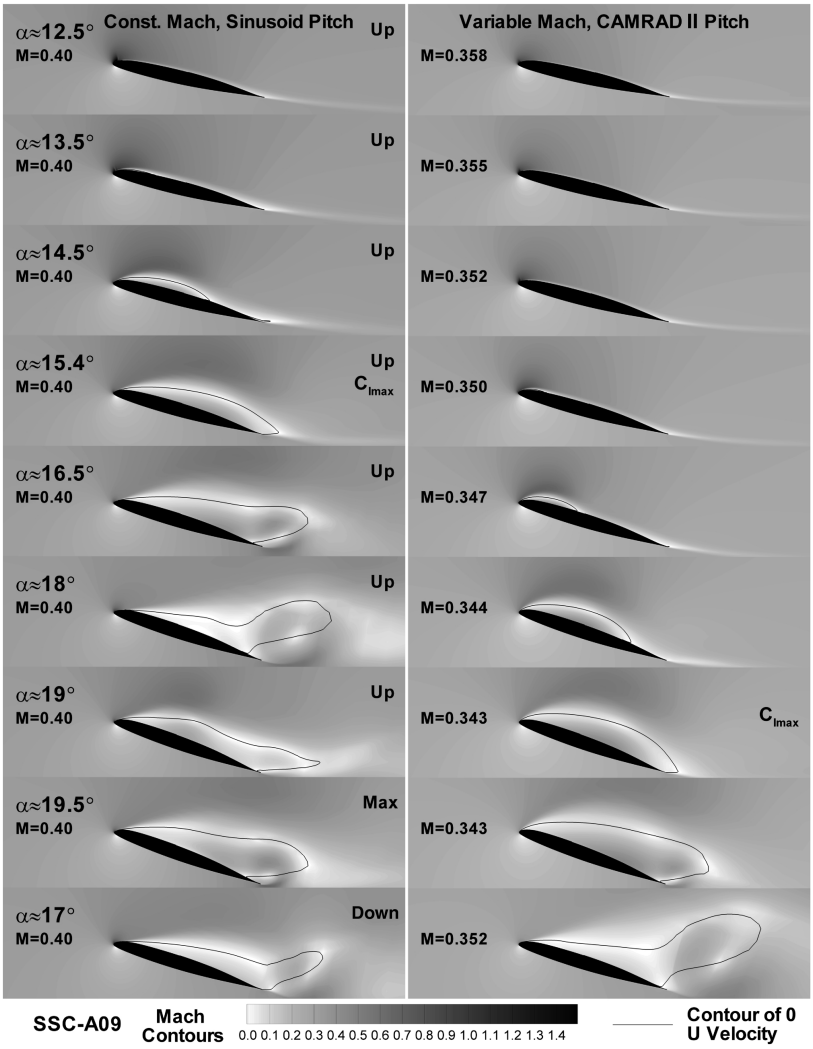

Fig. 11 Unsteady Mach contours for the baseline SSC-A09.

a dynamic stall vortex. The adaptive Spar85Defl10 section, however, shows no separation until the beginning of the downstroke. The higher $C_{l\max}$ produced by the SSC-A09 section is a result of the shedding of a more powerful dynamic stall vortex. The adaptive section should be capable of remaining attached to a higher angle of attack and lift coefficient.

To completely suppress the formation and passage of a dynamic stall vortex, the chordwise extent of the droop and maximum droop

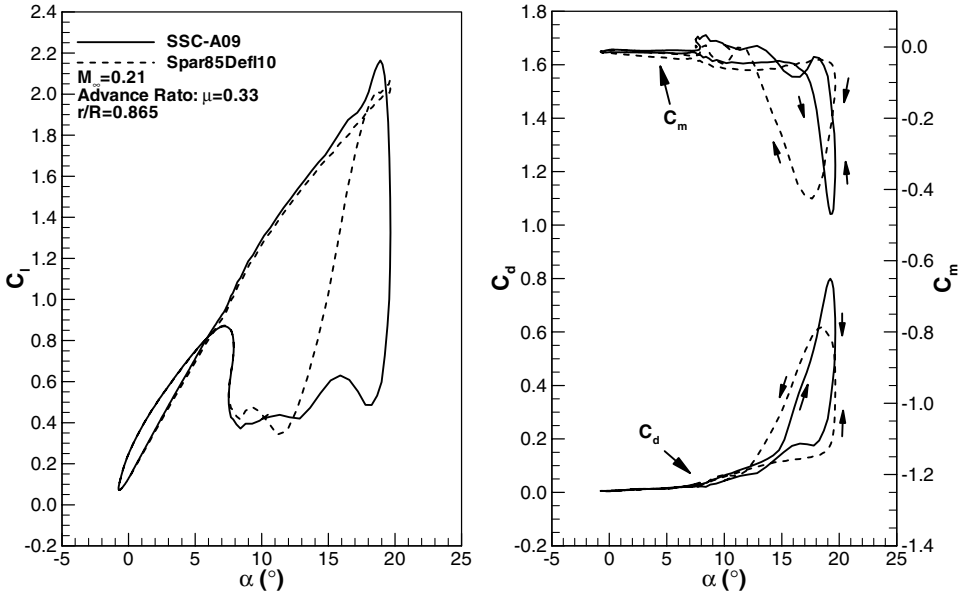

Fig. 12 Unsteady results for the variable Mach and CAMRAD II pitch cycle.

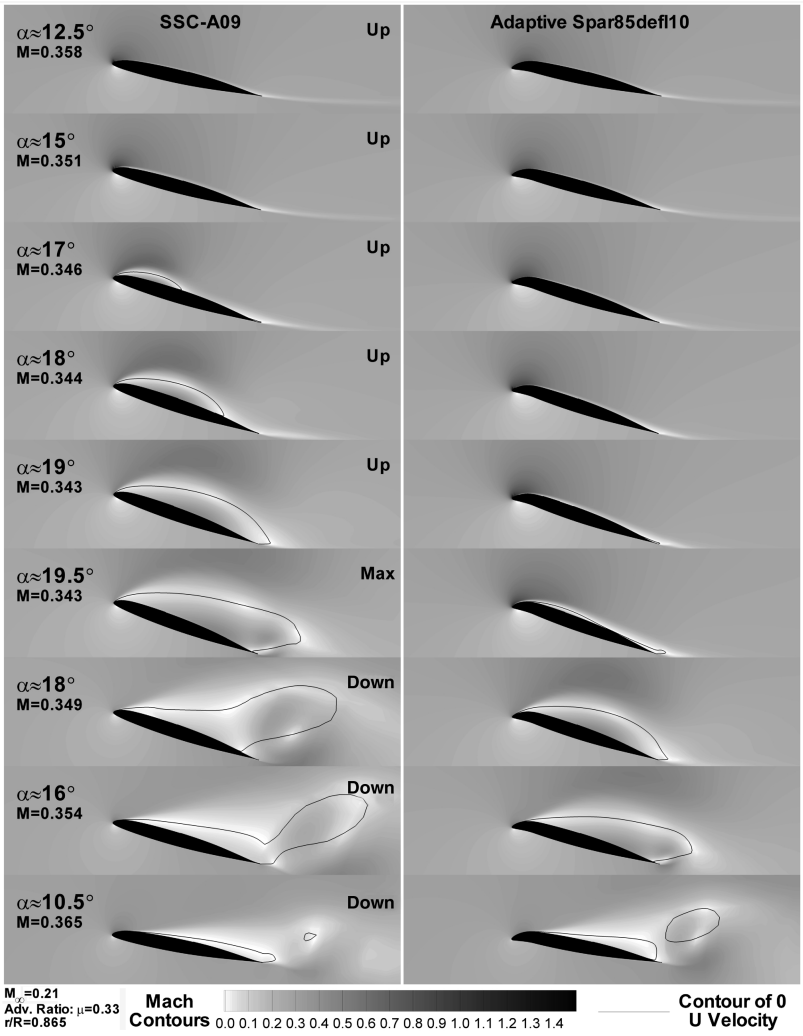

Fig. 13 Unsteady Mach contours for the variable Mach and CAMRAD II pitch cycle.

angle could be increased. Chandrasekhara et al. [7] used a 25% chord leading-edge flap with a maximum deflection of 20 deg. Instead, some slight aerodynamic optimization of the upper surface leading-edge region of the Spar85Defl10 section was performed. The new modified adaptive section is termed the Opt1 section. One of the significant benefits of using compliant structures is the ability to reshape the section in addition to a simple droop. Like the Spar85Defl10 section, the Opt1 section also produces 10 deg of droop while moving the D-spar aft to the 8.5% chord location. As the Opt1 section droops, however, the leading-edge contour is reshaped slightly to reduce the magnitude of the leading-edge pressure peak. Unsteady results for the SSC-A09, Spar85Defl10, and new Opt1 section for the variable Mach and CAMRAD II pitch cycle are shown in Fig. 14. From Fig. 14, the Opt1 results produce a $C_{l\max}$ equivalent to the Spar85Defl10 section, but without the formation and separation of the dynamic stall vortex on the downstroke. No large reduction in C_l and increase in C_d or C_m are noted. The Opt1 section is an aerodynamically refined version of the Spar85Defl10 section. Whereas both the SSC-A09 and Spar85Defl10 section produce a dynamic stall vortex for the α range shown, the Opt1 section does not. The Opt1 section could therefore be pushed to a higher α before a dynamic stall vortex is observed. As a result, the Opt1 section should theoretically have a higher $C_{l\max}$ than the SSC-A09 and Spar85Defl10 sections with an increased pitch range.

The unsteady dynamic results presented for the Spar85Defl10 and Opt1 sections appear to be promising from an aerodynamic standpoint. The variable Mach and prescribed CAMRAD II pitch cycle show results significantly different than that observed using the traditional constant Mach and sinusoidal α variation. Although still lacking the 3-D flowfield aspects of the finite rotor blade and blade/blade interactions, these more accurate representations of the blade environment provide a more accurate analysis tool than the traditional forced oscillation analysis.

Conclusions

An adaptive variable camber airfoil designed to alleviate, or greatly reduce, the negative effects of dynamic stall on rotorcraft blades has been investigated numerically. The variable camber airfoil is designed to deform dynamically in the form of a leading-edge nose droop throughout the rotorcraft pitch cycle allowing for an optimized blade section on both the advancing and retreating blades.

The OVERFLOW 1.8ab code was modified to include a dynamically deforming grid and variable Mach capability. These modifications allowed the baseline and adaptive rotor blade sections to be studied in a more realistic rotorcraft environment as compared with traditional forced oscillation analysis. The variable Mach capability simulates the rotational aspect of the rotorcraft flowfield in forward flight. In addition to the variable Mach number, a prescribed pitch cycle derived from CAMRAD II analyses were also investigated. The variable Mach/CAMRAD II pitch variation produced results significantly different than the traditional constant Mach/sinusoid pitch cycle forced oscillation.

Numerical predictions from this study have shown that the adaptive drooping design concept holds significant aerodynamic promise. Both the Spar85Defl10 and Opt1 sections were shown to significantly delay or eliminate the formation and shedding of the dynamic stall vortex as compared with the baseline SSC-A09

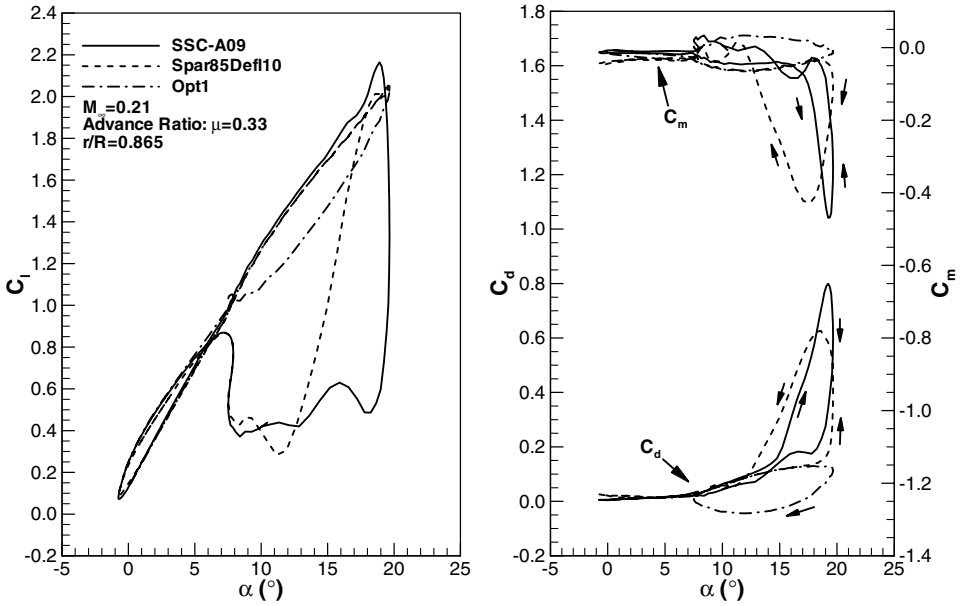

Fig. 14 Comparison of unsteady results for the SSC-A09, Spar85Defl10, and Opt1 sections for the variable Mach and CAMRAD II pitch cycle.

section. Results obtained to date indicate that the variable droop/camber compliant leading-edge system can achieve a higher $C_{l\max}$ than a baseline section, or eliminate the dynamic stall vortex at a C_l equivalent to the baseline section $C_{l\max}$ while maintaining the baseline section's high Mach number advancing blade characteristics. The significant challenge remains in the structural design and actuation of a realizable adaptive compliant rotor blade.

Acknowledgments

This work was supported by the Army Aeroflightdynamics Directorate at NASA Ames Research Center under a Phase II Small Business Innovation Research award, contract number W911W6-04-C-0001. The author would like to thank the technical monitor Preston Martin for his support and many contributions throughout this program and Hyeonsoo Yeo for the UH-60A CAMRAD II results. The author would also like to thank Mark Potsdam of the Army Aeroflightdynamics Directorate for many conversations, suggestions, and insights concerning the black arts, and also for his geometric conservation law code subroutines. Finally, the author would also like to thank Pieter Buning of NASA Langley for his help and suggestions concerning the OVERFLOW code, and Joel Hetrick of FlexSys Corporation for his compliant surface deformation routines.

References

[1] Gessow, A., and Myers, G., *Aerodynamics of the Helicopter*, Frederick Ungar Publishing, New York, 1952, pp. 250–267.

[2] Chandrasekhara, M., Wilder, M., and Carr, L., "Compressible Dynamic Stall Control Using a Shape Adaptive Airfoil," AIAA Paper 99-0650, Jan. 1999.

[3] Geissler, W., and Sobieczky, H., "Dynamic Stall Control By Variable Airfoil Camber," CP-522, AGARD, Aug. 1995, pp. 6.1–6.10.

[4] Yu, Y. H., Lee, S., McAlister, K. W., Tung, C., and Wang, C. M., "Dynamic Stall Control for Advanced Rotorcraft Applications," *AIAA Journal*, Vol. 33, No. 2, 1995, pp. 289–295.

[5] Reuster, J. G., Baeder, J. D., "Leading Edge Deformation for Dynamic Stall Control," AIAA Paper 2001-0120, Jan. 2001.

[6] Fink, D. A., Hawkey, T. J., Gaudreau, M. P. J., Wellman, B., and Ormiston, R. A., "Electromagnetic Actuator for Individual Blade Control," *56th Annual Forum*, American Helicopter Society, Virginia Beach, VA, May 2000.

[7] Chandrasekhara, M., Martin, P., and Tung, C., "Compressible Dynamic Stall Control Using a Variable Droop Leading-Edge Airfoil," *Journal of Aircraft*, Vol. 41, No. 4, 2004, pp. 862–869.

[8] "Advanced Fighter Technology Integration F-111 Mission Adaptive Wing," NASA CP-3055, April 1989.

[9] Ko, S., and McCroskey, W. J., "Computations of Unsteady Separating Flow over an Oscillating Airfoil," *AIAA Journal*, Vol. 35, No. 7, 1997, pp. 1235–1238.

[10] Ravindran, S., "Active Control of Flow Separation Over an Airfoil," NASA TM-1999-209838, Dec. 1999.

[11] Morton, S. A., Melville, R. B., and Visbal, M. R., "Accuracy and Coupling Issues of Aeroelastic Navier–Stokes Solutions on Deforming Meshes," *Journal of Aircraft*, Vol. 35, No. 5, 1998, pp. 798–805.

[12] Thomas, P. D., and Lombard, C. K., "Geometric Conservation Law and its Application to Flow Computations on Moving Grids," *AIAA Journal*, Vol. 17, No. 10, 1979, pp. 1030–1037.

[13] Obayashi, S., "Freestream Capturing for Moving Coordinates in Three Dimensions," *AIAA Journal*, Vol. 30, No. 4, 1992, pp. 1125–1128.

[14] Potsdam, M., Yeo, H., and Johnson, W., "Rotor Airloads Prediction Using Loose Aerodynamic/Structural Coupling," *Journal of Aircraft*, Vol. 43, No. 3, 2006, pp. 732–742.

[15] Wood, M. E., "Results from the Oscillatory Pitch Tests on the NACA 0012 Blade Section," Aircraft Research Association Memo 220, U.K., 1979.

[16] Johnson, W., "Rotorcraft Aerodynamics Models for a Comprehensive Analysis," *54th Annual Forum*, American Helicopter Society, Washington, D. C., May 1998.

[17] Bousman, W. G., "Airfoil Design and Rotorcraft Performance," *58th Annual Forum*, American Helicopter Society, Montreal, Canada, June 2002.

[18] Prouty, R. W., *Practical Helicopter Aerodynamics*, PJS Publications, Peoria, IL, 1982, pp. 26–31.